# An enhanced meshless numerical methodology for modelling pulsed laser ablation of aluminium

Zhihao Zhong , Sivakumar Kulasegaram , Emmanuel Brousseau [*]

*School of Engineering, Cardiff University, Cardiff, UK*

## ABSTRACT

Laser machining has become increasingly popular given the ability of this manufacturing technique to process a wide range of materials over multiple length scales, i.e., from the micro to the macroscale. In this work, a meshless numerical model based on Smooth Particle Hydrodynamics (SPH) was developed and tested to simulate pulsed laser ablation of aluminium in the nanosecond regime. In this model, the material removal mechanism was based on phase explosion and evaporation in contrast to existing, although still scarce, SPH-based models of laser ablation. In particular, the distinguishing characteristic of the proposed model is that it not only predicts the surface recession due to phase explosion, but also captures the ablation depth due to evaporation at low laser intensity regime. In addition, compared to previous research reports where SPH was employed to simulate laser ablation, the model developed here also comprehensively considered the temperature dependence of the material thermophysical properties as well as the temperature and wavelength dependence of its optical properties. The predicted ablation depths of aluminium following single pulse irradiation were in good agreement with four experimental data sets from two independent experimental studies. These experimental data enabled testing the developed model over a wide range of laser parameters, specifically a pulse fluence value between 0.5 J/cm$^2$ and 46.5 J/cm$^2$, a pulse duration spanning from 0.5 ns to 35 ns and a wavelength for the incident laser comprised between 515 nm and 1064 nm.

## 1. Introduction

Laser machining is currently employed in an expanding range of sectors as it is becoming increasingly popular due to its unique advantages compared to traditional material removal technologies. As a flexible and contactless machining method, laser processing can deliver very low to extremely high energy from 1 kW to 100 kW within a pulse duration ranging between $10^{-3}$ s and $10^{-15}$ s to any substrate [1]. Laser ablation, as one of the possible laser processing applications, aims to remove material precisely with minimal damage to the workpiece. Laser ablation encompasses a range of more specific techniques such as laser surface cleaning and laser drilling, for instance. Three main material removal mechanisms have been presented in the literature to describe and model pulsed laser ablation [2]. First, evaporation is a basic material removal mechanism at various laser intensities and timescale. It has been regarded as the main material removal mechanism by some researchers when building numerical models of the process with a view to predict the laser ablation depth [3,4]. In particular, the evaporation rate in these reports is calculated based on the surface temperature using the

Hertz-Knudsen equation. Second, normal boiling has also been considered as a potential removal mechanism. However, it is unlikely to take place on the nanosecond time scale, as the motion of bubbles is too slow to have any physical significance in this case [5]. Third, in addition to evaporation and normal boiling mechanisms, phase explosion, or explosive boiling, is also a possible material removal phenomenon, which has already been observed during nanosecond pulsed laser ablation [6]. In the case of phase explosion, the liquid metal is superheated and when its temperature becomes close to 90 % of its critical temperature, the heterogeneous nucleation rate increases sharply, resulting in breaking down of the liquid phase near the surface and the subsequent ejection of liquid and vapour. When considering nanosecond pulsed laser ablation, phase explosion has been regarded as an efficient material removal mechanism [2].

To optimise machining parameters and predict the laser ablation depth, some researchers have proposed the application of finite element (FE) [3,7] and finite volume (FV) based computational models [8]. Although such mesh-based numerical models can generally produce reasonable outcomes, they may not always be suitable for simulating

---

laser ablation as the process involves free surfaces and multiple phase interfaces [9]. Furthermore, these mesh-based methods may lose accuracy when the studied domain is on the micrometre or sub-micrometre scale [10]. To overcome the aforementioned limitations of mesh-based modelling techniques, Smooth Particle Hydrodynamics (SPH), a Lagrangian-based mesh-free method, has been applied by a few researchers in recent years to simulate laser processing. Initially proposed by Lucy [11] and Gingold and Monaghan [12] in 1977 to capture astrophysical phenomena in the free boundary domain, SPH has been utilised for simulating various engineering problems over the last three decades. In the case of laser processing, SPH has been applied for the simulation of laser welding [13,14] and laser powder bed fusion additive manufacturing [9,15] given the ability of this modelling approach to capture highly non-linear deformation and complex particle motion. In comparison, reports of SPH models for laser ablation are rarer despite the intrinsic advantage of SPH to simulate this specific process as well. In 2013, Muhammad et al. proposed a simple SPH model to investigate laser drilling and showed that the technique bears some interesting potential to produce simulation results [16]. It should be noted however, that the thermal and optical properties of the irradiated material were assumed to be constant by these authors and that this can result in a lack of simulation accuracy. A few years later, Cao and Shin [17] built a novel multiscale hydrodynamics model combined with molecular dynamics and SPH to investigate phase explosion under high laser fluence irradiation and simulated melt ejection from the melt pool for aluminium and copper workpieces. With this approach, the data interfaces and the boundary conditions between various parts of the developed algorithm may potentially reduce the accuracy of the combined model. In 2017, Alshaer et al. [10] proposed a new SPH model to predict the ablation depth of cavities created by processing an aluminium workpiece with nanosecond pulsed laser irradiation. The material removal mechanism considered by these authors was based on the normal boiling scenario and neglected the latent heat of fusion and evaporation. Besides, the material properties were also assumed to be constant, i.e., not temperature dependent. It is argued that these factors can have an impact on the accuracy of the results and may not reflect the realistic scenario of the laser ablation process.

Based on the somewhat limited body of current research on the SPH simulation of laser ablation, it can be said that there is still a need to develop an enhanced and robust SPH computational model for this specific laser process. In particular, the material removal mechanism considered in the existing SPH models of laser ablation was normal boiling, whereas evaporation and phase explosion could be the most realistic mechanism, especially at the nanosecond time scale. Hence, it would be prudent to develop a computational model for the laser ablation process based on evaporation and phase explosion to explore the potential of the SPH method in predicting the depth of generated craters. For this reason, such a model was implemented and tested in this paper. In addition, to further enhance the proposed SPH model, temperature and wavelength dependent material properties were also taken into account.

## 2. SPH methodology

In SPH simulations, the computational domain is divided into a set of particles, each assigned with a certain mass, density, position, velocity, and other physical properties. The interactions between each particle are controlled by the discrete SPH form of governing equations within the range of the smoothing length. Fig. 1 shows the particle $i$ and its surrounding particles $j$ with their interaction zone defined by a kernel function.

A continuous function $f(\mathbf{r})$ can be transferred into a fundamental SPH discretisation form through two approximations, namely the kernel approximation and the particle approximation [18]. With the kernel approximation, the integral and rigorous smoothing form of a function,
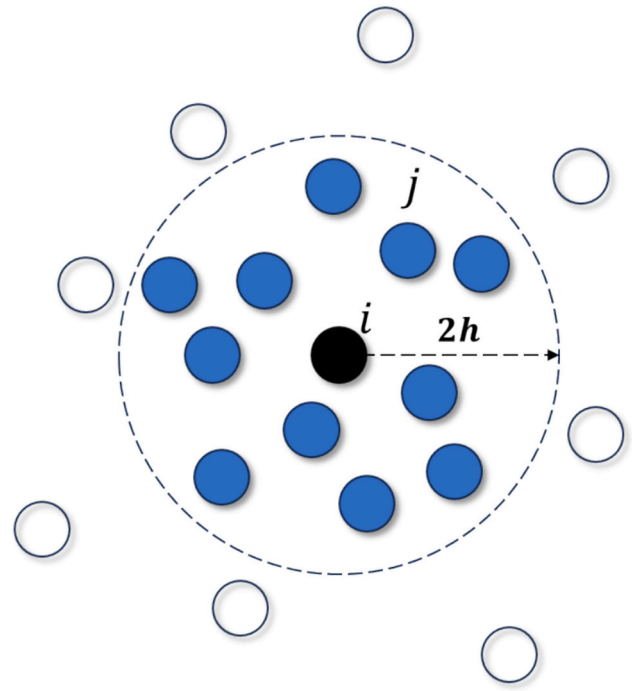


**Fig. 1.** Schematic of neighbouring particles $j$ and $i$ interaction within a kernel support.

$$f(\mathbf{r}) = \int \delta(\mathbf{r} - \mathbf{r}')f(\mathbf{r}')d\mathbf{r}' \tag{1}$$

is converted into a finite form via replacing the Dirac delta function $\delta(\mathbf{r} - \mathbf{r}')$ by a smoothing function, $W(\mathbf{r} - \mathbf{r}', h)$, as expressed below:

$$\langle f(\mathbf{r}) \rangle = \int W(\mathbf{r} - \mathbf{r}', h)f(\mathbf{r}')d\mathbf{r}' \tag{2}$$

In the above equation, $\mathbf{r}$ is a position vector, and $h$ is the smoothing length, which is used to determine the influence of each particle on its surrounding particles based on their inter-particle distances. Next, the continuous form of the kernel approximate of a function is transferred into a discrete summation over the neighbouring particles with the particle approximation, as follows:

$$\langle f(\mathbf{r}_i) \rangle = \sum_{j}^{N} W_{ij} f(\mathbf{r}_j) \frac{m_j}{\rho_j} \tag{3}$$

where $N$ is the total number of neighbouring particles, $W_{ij} = W(\mathbf{r}_i - \mathbf{r}_j, h)$ is the smoothing function and $m_j$ and $\rho_j$ are the mass and density respectively of the neighbouring particles. From the Eq. (3), the SPH discretisation of the derivative of a function $f(\mathbf{r})$ can be obtained by transferring the differential onto the smoothing function as follows:

$$\langle \nabla f(\mathbf{r}_i) \rangle = \sum_{j}^{N} f(\mathbf{r}_j) \frac{m_j}{\rho_j} \nabla_i W_{ij} \tag{4}$$

Through the kernel and particle approximations, the SPH form of governing equations of specific engineering problems can be formulated. Several kernel functions are available in the literature; the Gaussian kernel, the Quadratic kernel, and the Quintic kernel to name a few. In this work, the Cubic Spline kernel function defined by Monaghan [19] was employed due to its compact support, continuous second derivative and the order of accuracy [19]. This Cubic Spline kernel function can be expressed as below:

$$f(x) = a_D \begin{cases} 1 - \dfrac{3}{2}q^2 + \dfrac{3}{4}q^3, & 0 \leq q \leq 1 \\ \dfrac{1}{4}(2-q)^3 & 1 \leq q \leq 2 \\ 0 & q \geq 2 \end{cases} \tag{5}$$

where $q = r_{ij}/h$ for which $r_{ij}$ is the distance between particle $i$ and particle $j$, and $a_D$ is a constant ($a_D = 10/\left(7\pi h^2\right)$ in 2D and $a_D = 1/\left(\pi h^3\right)$ in 3D).

## 3. Model description

### 3.1. Governing equations of laser source and heat transfer

The differential equation governing the heat transfer problem between the incident laser beam and the irradiated material can be expressed as follows:

$$C_p \frac{dT}{dt} = \frac{1}{\rho}\nabla(k\nabla T) + Q_{laser} - Q_{loss} \tag{6}$$

where $C_p$ is the heat capacity, $\rho$ is the density, $k$ is the thermal conductivity, $Q_{laser}$ is the laser heat source, and $Q_{loss}$ is the heat loss. The heat conduction term, $\frac{1}{\rho}\nabla(k\nabla T)$, can be written in SPH form as follows [20]:

$$C_{p,i}\frac{dT_i}{dt} = \sum_j \frac{m_j}{\rho_i \rho_j}\left(\frac{4k_i k_j}{k_i + k_j}\right)\left(\frac{T_i - T_j}{r_{ij}^2}\right)\boldsymbol{r}_{ij}\cdot\nabla_i W_{ij} \tag{7}$$

where $C_{p,i}$ is the heat capacity of particle $i$, $k_i$ and $k_j$ are the thermal conductivity of particle $i$ and particle $j$, respectively, $m_j$ is the mass of particle $j$, $r_{ij} = |\boldsymbol{r}_{ij}|$ is the distance between particle $i$ and $j$, and $\boldsymbol{r}_{ij}$ is the relative position vector. In this model, the particles on the top surface of the workpiece material are irradiated by the laser source and some portion of heat is lost due to convection and radiation. Therefore, in addition to the heat conduction term, the laser source and the heat loss term should be considered for these particles, as below:

$$C_{p,i}m_i\frac{dT_i}{dt} = \sum_j \frac{m_i m_j}{\rho_i \rho_j}\left(\frac{4k_i k_j}{k_i + k_j}\right)\left(\frac{T_i - T_j}{r_{ij}^2}\right)\boldsymbol{r}_{ij}\cdot\nabla_i W_{ij} + Q_{laser} - Q_{loss} \tag{8}$$

The heat loss term, $Q_{loss}$, is due to convection and radiation and is given by [16]:

$$Q_{loss} = A_p\left[h_c(T_s - T_0) + \varepsilon\sigma_B\left(T_s^4 - T_0^4\right)\right] \tag{9}$$

where $A_p$ is the surface area considered the heat loss, $T_s$ is the temperature of the surface particle, $T_0$ is the ambient temperature (assumed to be 300 K), $h_c = 20$ W/(m²·K) is the convection factor, $\varepsilon = 0.09$ is the emissivity, and $\sigma_B = 5.67 \times 10^{-8}$ W/(m²·K⁴) is the Stefan–Boltzmann coefficient. According to the Beer-Lambert law, the laser intensity absorbed by the workpiece material at a given depth is calculated as:

$$I(z) = (1-R)I_0(\bar{r}, t)[1 - exp(-\alpha z)] \tag{10}$$

where $R$ is the reflectivity, $I_0(\bar{r}, t)$ is the laser irradiance, $\bar{r}$ is the radial distance from the beam centre, $t$ is the time, $\alpha$ is the optical absorption coefficient and $z$ is the vertical distance into the workpiece material from the surface. At room temperature, the optical absorption coefficient of aluminium is in the order of $10^8$ m⁻¹, while the calculated minimum optical absorption coefficient of liquid aluminium below $0.8T_c$ is about $4.2 \times 10^7$ m⁻¹ (see subsequent Section 3.3). The particle spacing used in this model was 0.2 μm. Thus, the application of the Beer-Lambert law at a temperature below $0.8T_c$ results in up to 99.98 % of the laser energy being absorbed by one particle spacing, even at the minimum optical absorption coefficient. Hence, the laser energy can be approximated as being absorbed completely by one particle spacing when their

temperature is below $0.8T_c$. In addition, once the temperature of liquid particles is above $0.8T_c$, their semi-transparent optical property has been simulated by setting a high value of heat conductivity (further details are provided in the subsequent Section 3.3). Consequently, the laser source can be approximated as being only absorbed by one particle spacing at various temperatures, as follows:

$$Q_{laser} = \dot{A}_p(1-R)I_0(\bar{r}, t) \tag{11}$$

where $\dot{A}_p$ is the irradiated area. The simulated nanosecond pulsed laser source has a Gaussian intensity profile in time, which was approximated here with the following expression [21]:

$$I(t) = I_{max,t}\left(\frac{t}{t_{max}}\right)^7 exp\left[7\left(1 - \frac{t}{t_{max}}\right)\right] \tag{12}$$

where $I_{max,t}$ is the peak laser intensity during a laser pulse and $t_{max}$ is the time at which the laser irradiance reaches its peak value. In the SPH model developed here, the intensity in space was approximated to be homogeneous because the area irradiated by the simulated laser beam was $4 \times 4$ μm², which is significant smaller than the beam spot diameter in the experiments against which the SPH simulations were compared [22,23]. However, it should be noted that the experimentally measured ablation depth values are from the deepest point in the crater to the surface. Hence, the maximum laser intensity of the beam area was used in the developed SPH model to perform a viable comparison between the numerical results obtained in this work and the experimental data in [22,23]. Compared to the mesh-based numerical models, it is not straightforward to allocate the laser source to the particles in SPH computational domain. Additional numerical treatment is needed to determine the laser source absorbed by the particles. For instance, Alshaer et al. [10] and Muhammad et al. [16] used a particle-based method to identity the free surface particles and then activated the laser source on them. The computational step that identifies the free surface particle involves the calculation of position divergence of particles as:

$$\nabla\cdot\boldsymbol{r}_i = \sum_j \frac{m_j}{\rho_j}\boldsymbol{r}_{ji}\cdot\nabla_i W_{ij} \tag{13}$$

For a given particle $i$, the more surrounding particles $j$ it possesses, the higher value of $\nabla\cdot\boldsymbol{r}_i$. Typically, the number of neighbours for surface particles is less than that for interior particles. Therefore, a threshold of $\nabla\cdot\boldsymbol{r}_i = 2.4$ was set empirically to determine the surface particle [16]. If $\nabla\cdot\boldsymbol{r}_i < 2.4$, then the particle is considered to be on the specimen surface. This method is straightforward and effective in identifying the free surface when it is flat, and the particle motion is moderate. However, in cases where the surface of the sample is rough or the particle motion is more pronounced, this method may not be able to capture all the free surface particles because it relies on the divergence of particle position. In particular, when modelling the laser ablation using SPH, particles can be ejected forcefully from the target, and it may not be straightforward to capture these irradiated particles using this approach. Therefore, a more accurate method based on an algorithm similar to that presented in [9] was developed to activate the laser source for the particles. As shown in Fig. 2, the method involves three steps:

1. Partition the particle volume onto a 3-dimensional grid and record the volume fraction of each generated cube. In particular, the size of a cube is set as half of the particle spacing. Fig. 2 shows the working principle of the algorithm using a 2-dimensional projection, where a cube is represented as a square in this case. In particular, the squares, i.e., cubes, with a more pronounced coloration are those with a relatively higher volume fraction.
2. Apply the laser beam source from the top to the bottom of the grid and activate this source to each cube. For this step, it is possible to employ the Beer-Lambert law to account for the portion of laser

source absorbed by a given cube based on its equivalent thickness, namely the volume fraction multiplied by the cube thickness. Such an elaborated procedure can be found in [9]. However, it was not implemented in this study due to the limited resolution of the grid and the extremely high value of the optical absorption coefficient of the material considered here. In this paper, the laser source is approximated to be linearly absorbed by twice the cube thickness which corresponds to one particle spacing.

3. Transfer the laser source of the cubes back to the particles.

### 3.2. Material removal mechanism

As mentioned in the Introduction section, the evaporation and phase explosion could be the most feasible and realistic material removal mechanism in nanosecond laser ablation. Consequently, these were considered to be the material removal mechanisms to be taken into account in this research. At the beginning of phase explosion, a dense region of vapour bubbles is generated in the superheated melting pool due to a rapid homogeneous nucleation rate. Once the temperature of the superheated liquid is close to the critical temperature, the liquid phase breaks down, which results in the release of vapour and small-scale liquid droplets from the target surface [5]. In the case of aluminium, the homogeneous nucleation rate has been calculated by Marla et al. [8] and found to increase sharply for temperatures above 0.86 of the critical temperature. In another study, Mazzi et al. estimated the temperature ratio of aluminium for phase explosion on a nanosecond time scale to be 91 % of the critical temperature [24]. Therefore, in the present work, phase explosion is assumed to occur instantly when the liquid temperature increases to 91 % of the critical temperature. In particular, once the temperature of surface particle reaches this temperature threshold, the surface particle is assumed to be ejected instantly from the target with a one-dimensional Maxwellian velocity in the normal direction. The value of ejected velocity was approximated as [25]:

$$v = \sqrt{\frac{2k_b T}{\pi m_a}} \tag{14}$$

where $k_b$ is the Boltzmann constant and $m_a$ is the atomic mass. This equation is expected to be a good approximation when the surrounding pressure is much less than the vapour pressure [10]. Before the temperature increases to the threshold of phase explosion, evaporation could take place at the target surface, resulting in material removal due to evaporation. To capture the surface recession due to evaporation, the mass of surface particle is updated at every time step according to the evaporation rate. The evaporation rate is estimated by the Hertz-Knudsen equation as [21]:

$$\dot{m} = \beta \sqrt{\frac{m_a}{2\pi k_b T}} P_v \tag{15}$$

where $\dot{m}$ is the evaporation rate [kg/(m$^2$·s)], $\beta = 0.82$ is the vaporisation coefficient [21], and $P_v$ [Pa] is the evaporation pressure, which can be estimated from the simplified Clausius-Clapeyron equation as [26]:

$$lgP_v = A_0 - B_0/T \tag{16}$$

where $A_0$ and $B_0$ represent constants associated with material properties. For aluminium, $A_0 = 11.79$ and $B_0 = 1.594 \times 10^4$ [26].

### 3.3. Material properties

The material properties considered in this research included thermophysical and optical parameters. Thermophysical properties, including density, thermal conductivity, and heat capacity, were approximated to be function of temperature, while optical properties, namely reflectivity and optical absorption coefficient, were modelled as temperature and laser wavelength dependent. The reflectivity of solid aluminium was considered to be constant, while for the liquid phase, it was calculated using Fresnel equations [27]:

$$R(T) = \frac{[n_R(T) - 1]^2 + n_I^2(T)}{[n_R(T) + 1]^2 + n_I^2(T)} \tag{17}$$

where $n_R(T)$ and $n_I(T)$ are the real and imaginary parts of the refractive index, respectively. When the temperature of the liquid aluminium was below $0.8T_c$, the values of $n_R(T)$ and $n_I(T)$ were calculated as follows [4,27]:

$$n_R(T) = \left\{ \frac{1}{2} \left[ \left( 1 - \frac{c^2 \mu_0 \gamma \sigma}{\gamma^2 + w^2} \right) + \sqrt{\left( 1 - \frac{c^2 \mu_0 \gamma \sigma}{\gamma^2 + w^2} \right)^2 + \frac{c^4 \mu_0^2 \gamma^4 \sigma^2}{[\gamma^2 w + w^3]^2}} \right] \right\}^{\frac{1}{2}} \tag{18a}$$

$$n_I(T) = \left\{ \frac{1}{2} \left[ \left( \frac{c^2 \mu_0 \gamma \sigma}{\gamma^2 + w^2} - 1 \right) + \sqrt{\left( 1 - \frac{c^2 \mu_0 \gamma \sigma}{\gamma^2 + w^2} \right)^2 + \frac{c^4 \mu_0^2 \gamma^4 \sigma^2}{[\gamma^2 w + w^3]^2}} \right] \right\}^{\frac{1}{2}} \tag{18b}$$

When the liquid temperature of the aluminium workpiece was above $0.8T_c$, then the value of the real and imaginary parts of the refractive index were calculated with the expressions below [4]:

$$n_R(T) = \left\{ \frac{1}{2} \left[ \left( 1 - \frac{\gamma \sigma}{(\gamma^2 + w^2)\varepsilon_0} \right) + \sqrt{\left( 1 - \frac{\gamma \sigma}{(\gamma^2 + w^2)\varepsilon_0} \right)^2 + \frac{\gamma^4 \sigma^2}{[\gamma^2 w \varepsilon_0 + w^3 \varepsilon_0]^2}} \right] \right\}^{\frac{1}{2}} \tag{19a}$$

$$n_I(T) = \left\{ \frac{1}{2} \left[ \left( \frac{\gamma \sigma}{(\gamma^2 + w^2)\varepsilon_0} - 1 \right) + \sqrt{\left( 1 - \frac{\gamma \sigma}{(\gamma^2 + w^2)\varepsilon_0} \right)^2 + \frac{\gamma^4 \sigma^2}{[\gamma^2 w \varepsilon_0 + w^3 \varepsilon_0]^2}} \right] \right\}^{\frac{1}{2}} \tag{19b}$$

where $c$ is the speed of light, $\sigma$ is the electrical conductivity, $\mu_0$ is the vacuum permeability, $\varepsilon_0$ is the vacuum permittivity, $w = 2\pi c/\lambda$ is the laser frequency at wavelength $\lambda$, and $\gamma$ is the electron collision frequency, which can be calculated from the simple Drude model [27]. Finally, the optical absorption coefficient below $0.8T_c$ was calculated as [4,8,27]:

$$\alpha = \frac{4\pi n_I(T)}{\lambda} \tag{20}$$

The material properties used in this model are summarised in Table 1. It should be noted that once the liquid temperature approaches the critical temperature, i.e., above $0.8T_c$, a significant reduction of electron density occurs, which can make the liquid to transform into a dielectric liquid, and as a result become semi-transparent to the incident laser [21]. Furthermore, with the increase of dielectric liquid temperature to $0.9T_c$, the dielectric liquid could become even more transparent
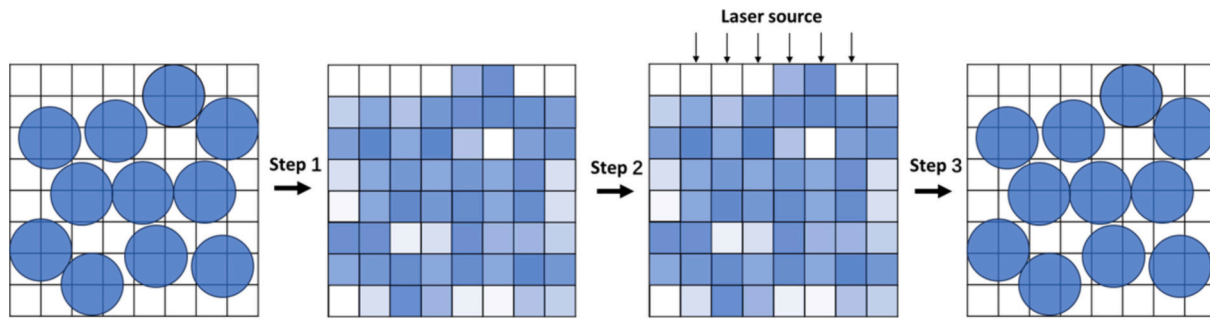
**Fig. 2.** Adopted algorithm for activating the laser source to particles.

to the incident laser [28]. However, it is not straightforward to quantify the semi-transparent property of the dielectric liquid. Hence, to simulate this phenomenon, a simple assumption is proposed here. In particular, when the temperature of the liquid phase is above $0.8T_c$, its heat conductivity is assumed to be one order of magnitude greater than the value of solid aluminium, i.e., 2000 W/(m·K). The reflectivity of the target is one of the most sensitive material properties for laser processing as it determines the laser energy absorption rate. The calculated reflectivity and optical absorption coefficient of liquid aluminium at 532 nm and 1064 nm wavelength are shown in Figs. 3 and 4, respectively.

*3.4. Numerical implementation*

The developed SPH meshless numerical model was implemented using the modified open-source Fortran code 'SPHysics' [33], which was originally created to simulate water flow. To adapt this code for laser ablation simulations, the governing equations and material properties presented in Sections 3.1 to 3.3 were incorporated into the Fortran code. In a previous research, Alshaer et al. [10] conducted a transient heat transfer analysis to investigate the optimum particle spacing to be used in SPH model. It was found that the simulated temperature values obtained from SPH model with 0.2 µm particle spacing were in good agreement with the analytical results [10]. Hence, in this study, a 3-D computational domain of dimension $4.8 \times 4.8 \times 10.4$ µm³, which comprised 29,952 particles with particle spacing of 0.2 µm between them, was created. The domain included two layers of thermal boundary particles located on the side and bottom surfaces. These boundaries were used to cool the adjacent particles by heat conduction. This is realistic for many laser material processing scenarios given that the workpiece can act as a heat sink as it is normally much larger than the laser spot size in practice. As mentioned earlier, the laser irradiance area was set to be

$4 \times 4$ µm², not including the boundary particles. At the beginning of the simulation, all particles were assumed to be at room temperature. Furthermore, a variable time step with maximum step size set at $5 \times 10^{-12}$ s was used in this work to ensure that the temperature change and the mass loss due to evaporation between two consecutive numerical iterations lied within a small range. More specifically, the maximum temperature change permitted was 30 K, and the mass loss permitted was <0.1 % of the particle mass before evaporation took place. Further details of the computer implementation are given in Appendix A.

## 4. Simulation results and comparisons with experimental data

The temperature evolution in time of the aluminium target for a 10 ns pulse at 515 nm wavelength and for a fluence of 7.5 J/cm² is shown in Fig. 5. In particular, this figure shows the temperature history at the centre of the beam, from the irradiated surface down to 0.8 µm in depth. The physical properties of the ejected aluminium, which is a highly compressed vapour mixed with small liquid droplets, are not available in the literature. Therefore, once the particle is ejected from the target, its temperature and velocity are assumed to be constant and is no longer influenced by the surrounding computational domain. Besides, the governing field equations are not employed in the presented model due to the uncertainty of physical properties of the superheated liquid during phase explosion. According to Eq. (14), the velocity of the ejected material at $0.91T_c$, can be calculated and was found to be around 1130 m/s, which is the same order of magnitude as the experimentally measured values in [34], i.e., from 1800 to 7000 m/s. Once material is expelled from the target, further interaction with the laser beam may keep increasing the vapour velocity. As mentioned earlier, when the liquid temperature increases above $0.8T_c$, the liquid could become semi-transparent to laser beam. Hence, the expected surface temperature

**Table 1**
Material parameters used in this study.

| Parameter | Temperature | Value | Units |
|---|---|---|---|
| Melting temperature ($T_m$) | | 933 [27] | K |
| Critical temperature ($T_c$) | | 7164 [29] | K |
| Critical density ($\rho_c$) | | 300 [29] | K |
| Latent heat of fusion ($L_m$) | | $3.999 \times 10^5$ [30] | J/kg |
| Density ($\rho$) | $T \leq T_m$ | $2852.5 - 0.5116T$ [4] | Kg/m³ |
| | $T > T_m$ | $\rho_c \left[ 1 + 0.75 \left( 1 - \dfrac{T}{T_c} \right) + 6.5 \left( 1 - \dfrac{T}{T_c} \right)^{1/3} \right]$ [4,27] | |
| Thermal conductivity ($k$) | $T \leq 400$ | $226.67 + 0.033T$ [4] | W/(m·K) |
| | $400 < T < T_m$ | $226.6 - 0.055T$ [4] | |
| | $T_m \leq T < 0.8T_c$ | $2.45T/(12.4729 + 1.3605 \times 10^{-2}T)$ [4] | |
| Specific heat capacity ($C_p$) | $T \leq T_m$ | $0.5203T + 643.9$ [31] | J/(kg·K) |
| | $T > T_m$ | $1160$ [31] | |
| Electrical conductivity ($\sigma$) | $T > T_m$ | $3 \times 10^4 \left[ 1 + 110 \left( 1 - \dfrac{T}{T_c} \right)^{3.6} + 52 \left( 1 - \dfrac{T}{T_c} \right)^{0.9} \right]$ [8] | S/m |
| Reflectivity ($R$) | $T \leq T_m$ | 0.92 [32] | |
| | $T > T_m$ | Eqs. (17)—(19a), (19b) | |
| Optical absorption coefficient ($\alpha$) | $T_m < T < 0.8T_c$ | Eq. (20) | |
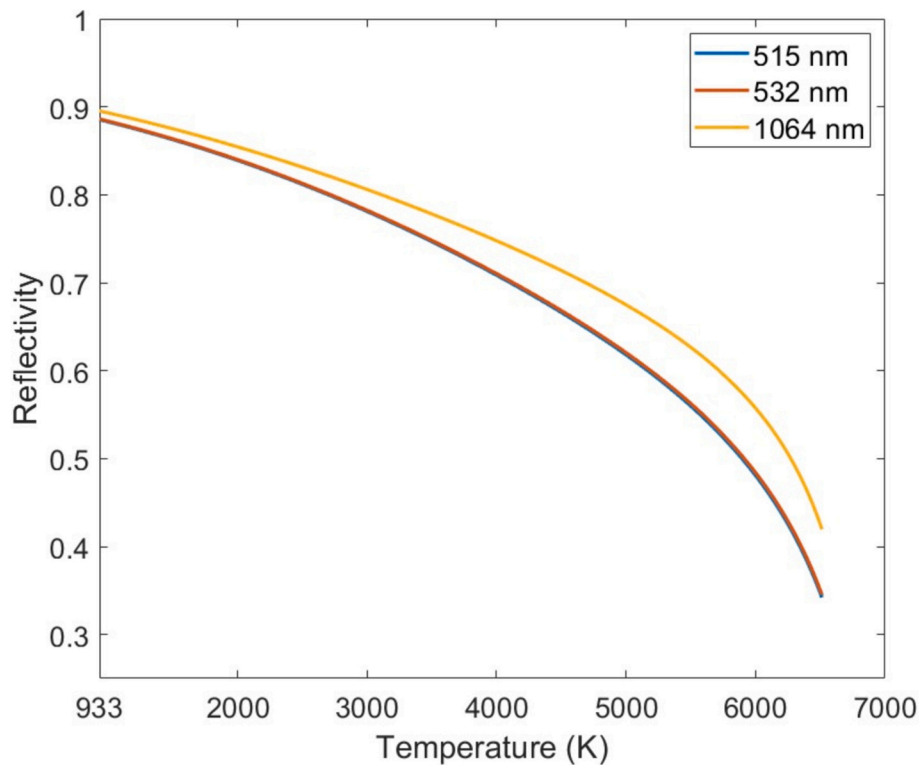
**Fig. 3.** Calculated reflectivity of aluminium as a function of temperature for wavelengths of 515 nm, 532 nm and 1064 nm.
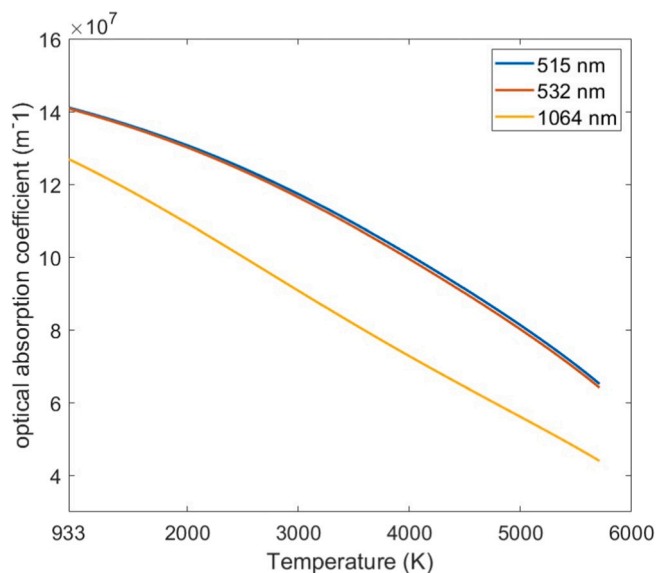


**Fig. 4.** Calculated optical absorption coefficient of aluminium as a function of temperature for wavelengths of 515 nm, 532 nm and 1064 nm.

increase can be slightly lower between $0.8T_c$ and $0.91T_c$, as shown in Fig. 5.

Fig. 6 illustrates the 3-D view and the corresponding side view of laser ablation evolution within the aluminium target at different times, i. e., $t = 4, 5, 6, 8$ and 10 ns. As the laser temporal intensity is Gaussian, the laser irradiance is higher in the middle of the pulse duration, which results in the surface recession occurring primarily after 5 ns.

The simulated ablation depths obtained from the proposed model were compared with experimental data in [22,23], which collectively cover a wide range of laser wavelength, pulse duration and laser fluence

values. Fig. 7 shows the predicted ablation depths under fluence values between 5 J/cm$^2$ and 35 J/cm$^2$ using a 10 ns pulse at 515 nm laser wavelength. In the reported experiments, lasers with two scan speeds were employed to irradiate the target. The experimental data with triangular markers presented in Fig. 7 were obtained with a laser at a high scan speed, which could ensure the irradiated areas did not overlap. Nevertheless, the data with square markers are the estimated single pulsed ablation depth from craters created with multiple pulses for which the measured depth was divided by the number of pulses. As a low scan speed was employed to irradiate the target, it results in the overlap of irradiated areas. It can be found that the ablation depths created by a single pulse is greater than the estimated single pulsed ablation depths from multiple pulses at the corresponding laser fluence. This could be due to the fact that the shielding effect of ejected material is greater in the case of multiple pulse irradiation, as the authors commented in [22]. As shown in Fig. 7, the magenta line is the simulated single ablation depths obtained from a previously reported SPH model [10]. While these results are in agreement with the multi-pulse experiment data to some extent, it may not be viable to compare the simulated single-pulse ablation depths with multi-pulse experiment data. Moreover, when these results are compared with the single-pulse experiment data, a large difference can be found. Using the SPH model developed in this work, the predicted single-pulse ablation depths have a good agreement with the corresponding single-pulse experimental data. At high laser fluence, the predicted ablation depths tend to be overestimated compared to experimental data. This could be due to the shielding effects of the ejected material, as the shielding effects could be greater at higher laser intensity. Hence, the rate of increase of experimental ablation depths can be reduced with the increase of laser intensity. This phenomenon can be observed in numerous nanosecond laser ablation experiments of aluminium [22,34–37]. Considering the factors mentioned above, it can be said that the simulated crater depths are still in reasonable agreement with the experiment data obtained from [22].

Additionally, another laser ablation experiment of aluminium with 1064 nm laser wavelength and a 0.5 ns pulse duration were also
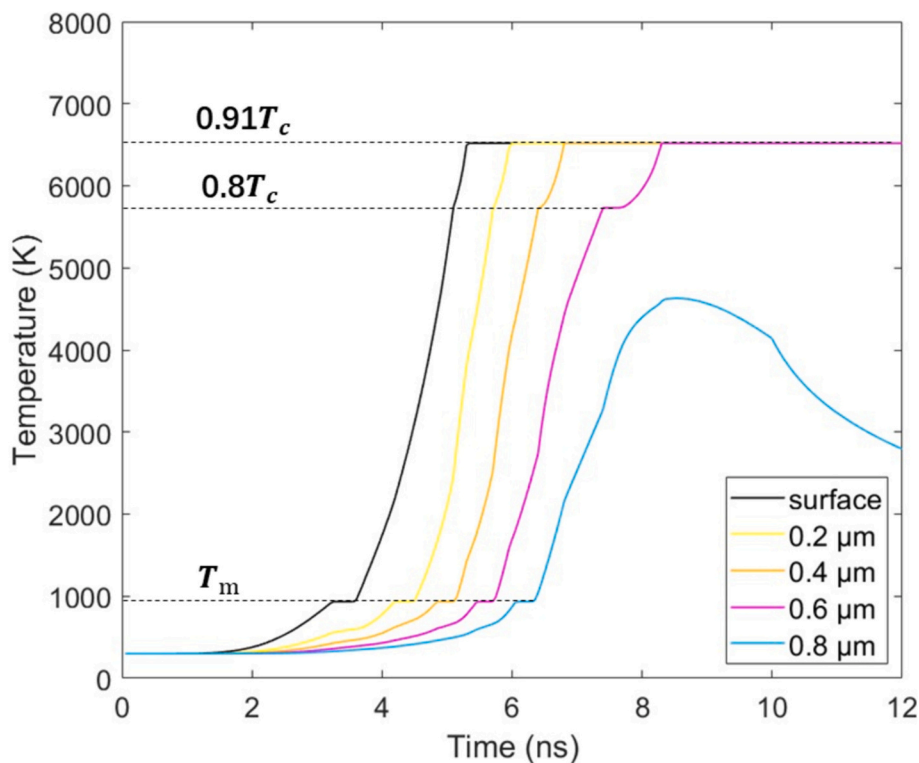
**Fig. 5.** Temperature evolution in time from the aluminium surface to 0.8 μm in depth along the axis corresponding to the centre of the beam for a laser wavelength of 515 nm, a fluence of 7.5 J/cm$^2$ and a pulse duration of 10 ns.
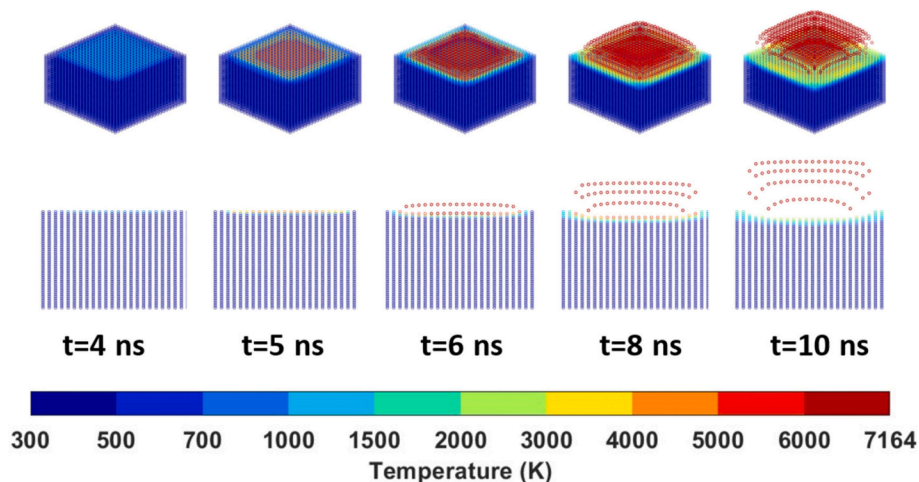


**Fig. 6.** 3-D view and corresponding side view of the simulated laser ablation evolution within the aluminium target using a laser wavelength of 515 nm, a fluence 7.5 J/cm$^2$ and a pulse duration of 10 ns.

reported in [22]. It should be noted that the ablation depths in that experiment were created with a high laser scan speed to avoid pulse overlap. Fig. 8 shows the predicted ablation depths under fluence values between 0.5 J/cm$^2$ and 20 J/cm$^2$, and the corresponding experimental data. Due to the short pulse duration, i.e., 0.5 ns, an extremely high laser intensity is reached between 5 J/cm$^2$ and 20 J/cm$^2$, i.e., from 21.5 GW/cm$^2$ to 86.2 GW/cm$^2$, respectively. Consequently, when the temperature of the surface layer particles reaches the phase explosion threshold, the lower layer particles remain at solid phase, and the physical property of these particles is nearly unchanged. Therefore, the predicted laser ablation depth has a linear correlation with laser intensity.

Colina and co-workers conducted laser ablation experiments on aluminium using two laser systems, namely a 532 nm ND: YVO$_4$ laser

with 10 ns pulse duration and a 1064 nm ND: YAG laser with 35 ns pulses [23]. Besides, these experimental laser ablation depths were generated by irradiating the target with a single pulse. The predicted ablation depths for a range of fluence values from 8.7 J/cm$^2$ to 21.1 J/cm$^2$ corresponding to the experiments conducted with the ND: YVO$_4$ laser are shown in Fig. 9. It can be said that the simulation results obtained with the SPH model are in reasonably good agreement with the experiment data.

Fig. 10 illustrates the predicted ablation depths for fluence values between 9 J/cm$^2$ and 46.5 J/cm$^2$ for a 35 ns pulse at 1064 nm laser wavelength. This simulated data corresponds to the experiments also conducted by Colina and co-workers but with the ND: YAG laser system in this case [23]. The data indicated with the green square markers are
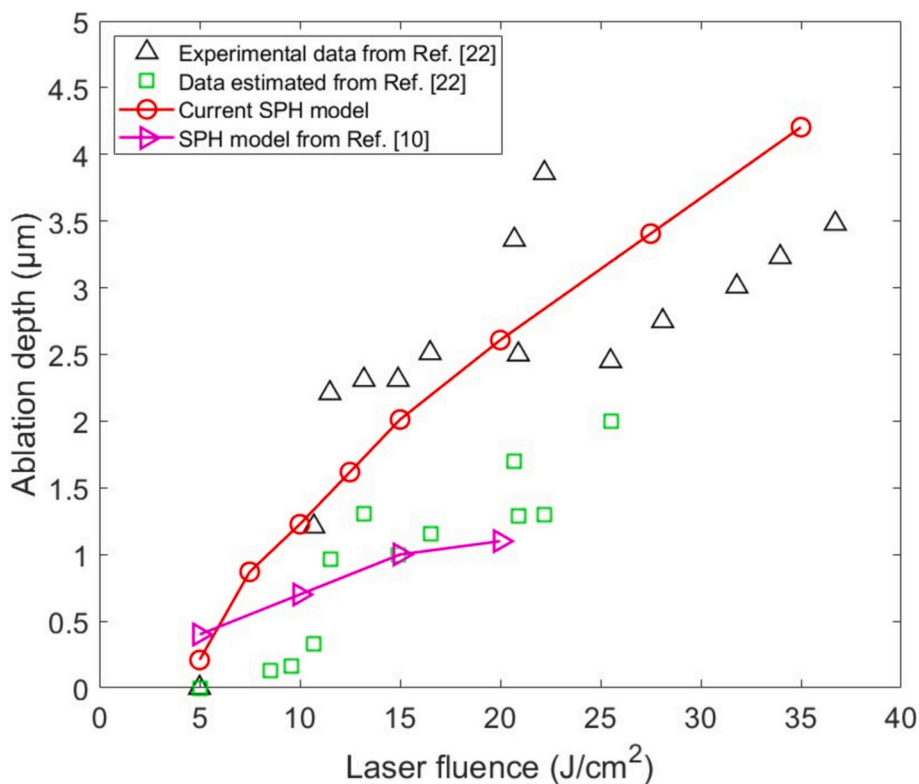
**Fig. 7.** Predicted ablation depth for a 10 ns pulse with fluence values ranging from 5 J/cm$^2$ to 35 J/cm$^2$ at 515 nm laser wavelength.
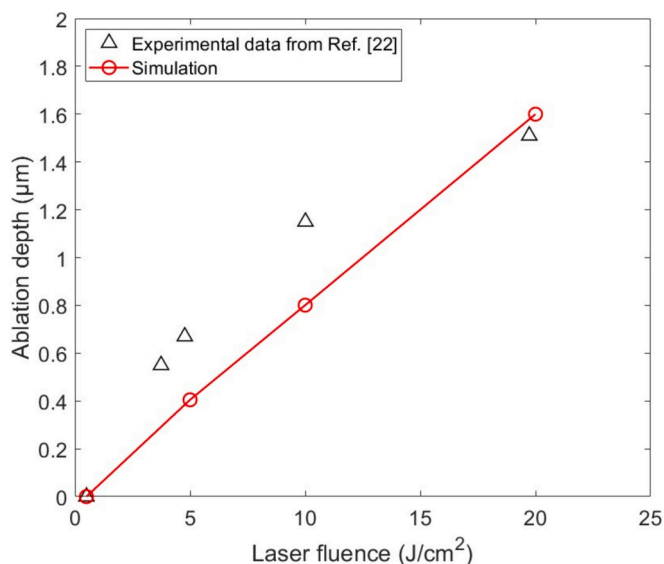


**Fig. 8.** Predicted ablation depth for a 0.5 ns pulse with fluence values ranging from 0.5 J/cm$^2$ to 20 J/cm$^2$ at 1064 nm laser wavelength.
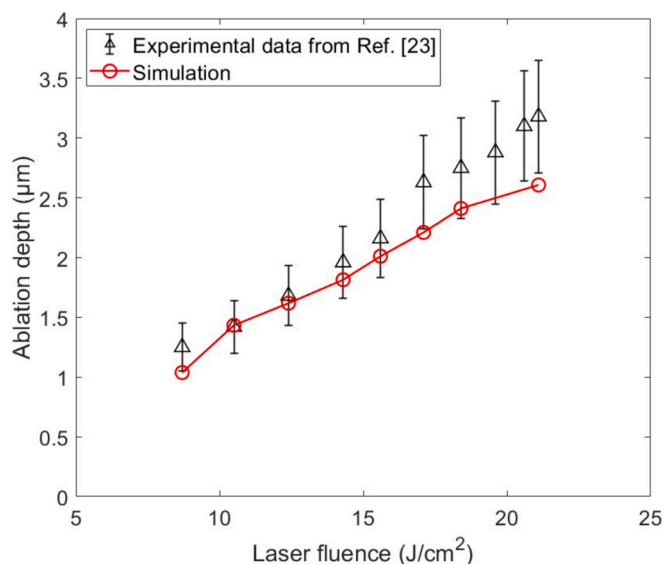


**Fig. 9.** Predicted ablation depths for a 10 ns pulse and for fluence values comprised between 8.7 J/cm$^2$ and 21.1 J/cm$^2$ at 532 nm laser wavelength.

the predicted ablation depths without considering the mass loss of surface particle due to evaporation and thus, phase explosion is modelled as the only material removal mechanism. When comparing the two simulation results, it can be noticed that the evaporation has significant influence on the laser ablation depth at lower laser intensity, and in contrast, the influence of phase explosion on the ablation depth gradually dominates with the increase of laser intensity. Moreover, the ablation depth due to phase explosion increases from 0 to 0.2 μm between 12.9 J/cm$^2$ and 17.4 J/cm$^2$ for which the corresponding peak laser intensity is from 0.79 GW/ cm$^2$ to 1.07 GW/ cm$^2$. This range of laser

intensity values is in good agreement with the phase explosion threshold obtained in [6,27]. As shown in Fig. 10, a better agreement can be observed between the simulation results and the experimental data at higher laser fluence, whereas a relatively larger difference exists at lower laser fluence. This difference may be due to the existing surface roughness of the workpiece. In particular, the roughness of the target in the experiment [23] is 0.7 μm, while the surface of the simulated target was assumed to be completely smooth. In the case of the low ablation depth, the estimated laser absorption rate may be underestimated, as the reflection of laser light between the surface roughness was not
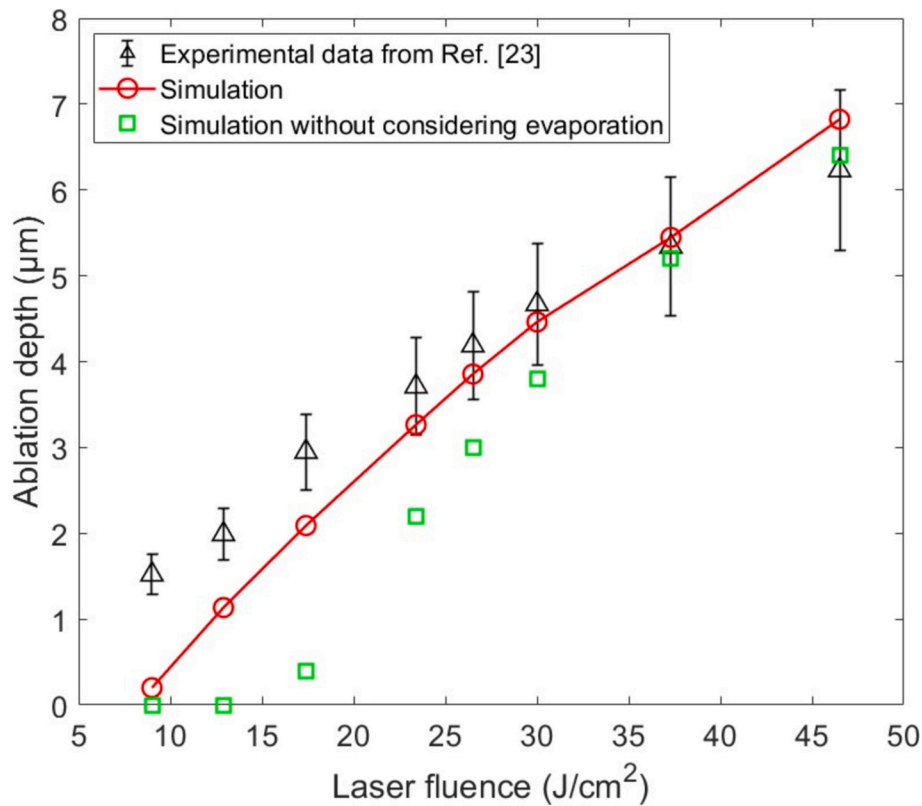
**Fig. 10.** Predicted ablation depths for a 35 ns pulse with laser fluence values between 9 J/cm$^2$ and 46.5 J/cm$^2$ and at 1064 nm laser wavelength.

considered in this model.

## 5. Conclusions

In this paper, a SPH-based numerical model of nanosecond pulsed laser ablation, which considered phase explosion and evaporation as the material removal mechanisms, was developed and implemented to predict the depth of single craters on an aluminium target. The proposed model comprehensively considered the temperature dependence of the target thermophysical properties as well as the temperature and wavelength dependence of its optical properties. Governing equations and varying material properties were implemented based on a Fortran open-source code. The predicted laser ablation depths were found to be in good agreement with four sets of experimental data obtained from two independent experimental studies, which together cover a wide range of laser fluence, pulse duration, and wavelength values. Besides, it was found that the evaporation has significant effect on the resulting ablation depth at low laser intensity regime, i.e., below 1 GW/ cm$^2$, whereas the effect of phase explosion dominates the ablation depth gradually with the increase in laser intensity. In addition, depending on specific experimental conditions, the shielding effect of ejected material above the melt pool could cause an attenuation of the incident laser intensity. The shielding effect, however, was neglected in the proposed model. It is

acknowledged that incorporating this effect into the developed numerical model should be an important step for future research.

## CRediT authorship contribution statement

**Zhihao Zhong:** Writing – original draft, Validation, Software, Methodology, Investigation, Formal analysis, Conceptualization. **Sivakumar Kulasegaram:** Writing – review & editing, Validation, Supervision, Methodology, Formal analysis, Conceptualization. **Emmanuel Brousseau:** Writing – review & editing, Validation, Supervision, Formal analysis, Conceptualization.

## Declaration of competing interest

The authors declare that they have no known competing financial interests or personal relationships that could have appeared to influence the work reported in this paper.

## Appendix A

Fig. 11 shows the flow chart of the computer implementation of the model presented in this study. MATLAB was used for data visualization.
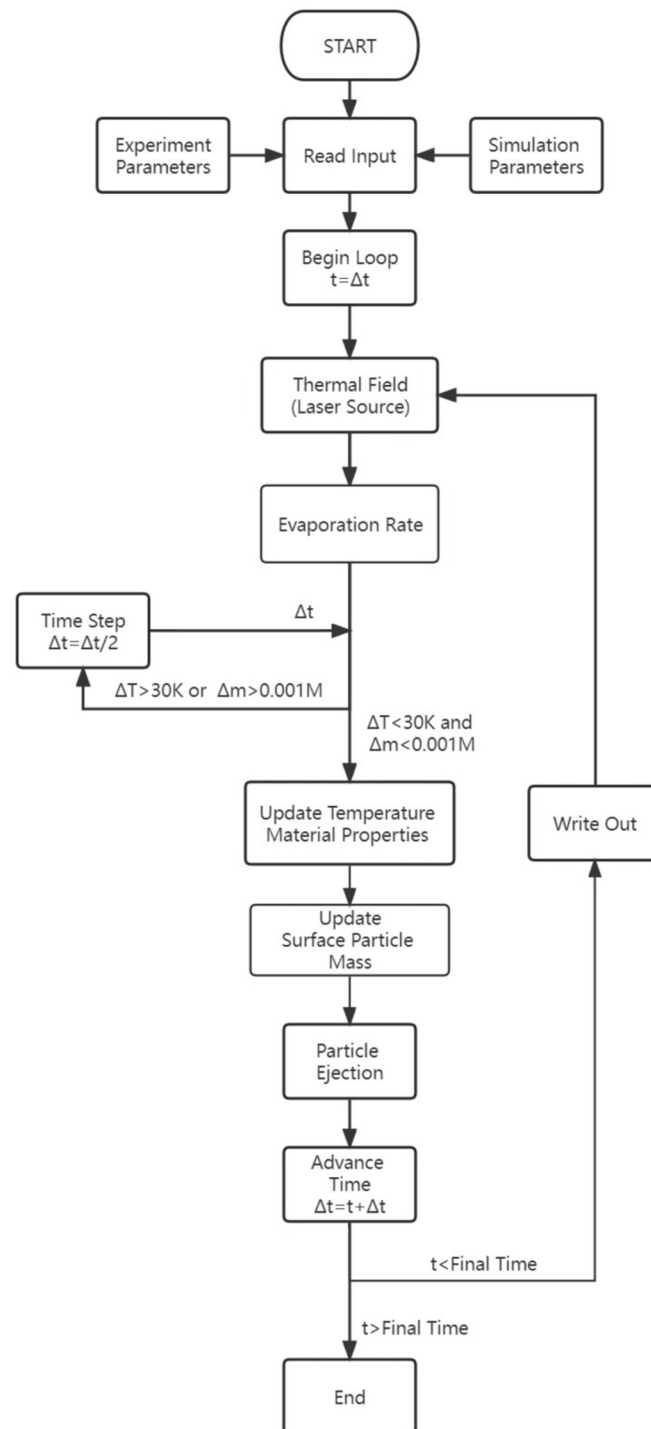
**Fig. 11.** Flow chart of computer implementation of the model described in this work.

## References

[1] Dutta Majumdar J, Manna I. Laser processing of materials. Sadhana 2003;28: 495–562.

[2] Kelly R, Miotello A. Contribution of vaporization and boiling to thermal-spike sputtering by ions or laser pulses. Physical Review E 1999;60(3):2616.

[3] Wang Y, Shen N, Befekadu GK, Pasiliao CL. Modeling pulsed laser ablation of aluminum with finite element analysis considering material moving front. International Journal of Heat and Mass Transfer 2017;113:1246–53.

[4] Zhang Y, Zhang D, Wu J, He Z, Deng X. A thermal model for nanosecond pulsed laser ablation of aluminum. AIP Advances 2017;7(7).

[5] Miotello A, Kelly R. Laser-induced phase explosion: new physical problems when a condensed phase approaches the thermodynamic critical temperature. Applied Physics A 1999;69(Suppl. 1):S67–73.

[6] Porneala C, Willis DA. Observation of nanosecond laser-induced phase explosion in aluminum. Appl Phys Lett 2006;89(21).

[7] Vasantgadkar NA, Bhandarkar UV, Joshi SS. A finite element model to predict the ablation depth in pulsed laser ablation. Thin Solid Films 2010;519(4):1421–30.

[8] Marla D, Bhandarkar UV, Joshi SS. A model of laser ablation with temperature-dependent material properties, vaporization, phase explosion and plasma shielding. Applied Physics A 2014;116:273–85.

[9] Russell MA, Souto-Iglesias A, Zohdi T. Numerical simulation of Laser Fusion Additive Manufacturing processes using the SPH method. Comput Methods Appl Mech Eng 2018;341:163–87.

[10] Alshaer AW, Rogers BD, Li L. Smoothed Particle Hydrodynamics (SPH) modelling of transient heat transfer in pulsed laser ablation of Al and associated free-surface problems. Comput Mater Sci 2017;127:161–79.

[11] Lucy LB. A numerical approach to the testing of the fission hypothesis. Astronomical Journal Dec. 1977;82:1013–24.

[12] Gingold RA, Monaghan JJ. Smoothed particle hydrodynamics: theory and application to non-spherical stars. Monthly Notices of the Royal Astronomical Society 1977;181(3):375–89.

[13] Hu H, Eberhard P. Thermomechanically coupled conduction mode laser welding simulations using smoothed particle hydrodynamics. Computational Particle Mechanics 2017;4:473–86.

[14] Li Z, Wang X, Yang H, Ni P, Li F, Liu H. Numerical studies on laser impact welding: smooth particle hydrodynamics (SPH), Eulerian, and SPH-Lagrange. Journal of Manufacturing Processes 2021;68:43–56.

[15] Qiu Y, Niu X, Song T, Shen M, Li W, Xu W. Three-dimensional numerical simulation of selective laser melting process based on SPH method. Journal of Manufacturing Processes 2021;71:224–36.

[16] Muhammad N, Rogers BD, Li L. Understanding the behaviour of pulsed laser dry and wet micromachining processes by multi-phase smoothed particle hydrodynamics (SPH) modelling. J Phys D Appl Phys 2013;46(9):095101.

[17] Cao Y, Shin YC. Multi-scale modeling of phase explosion in high fluence nanosecond laser ablation and clarification of ablation depth prediction criterion. Appl Surf Sci 2015;357:74–85.

[18] Liu MB, Liu G. Smoothed particle hydrodynamics (SPH): an overview and recent developments. Archives of Computational Methods in Engineering 2010;17:25–76.

[19] Monaghan JJ. Smoothed particle hydrodynamics. Annual Review of Astronomy and Astrophysics 1992;30(1):543–74.

[20] Monaghan JJ, Huppert HE, Worster MG. Solidification using smoothed particle hydrodynamics. J Comput Phys 2005;206(2):684–705.

[21] Porneala C, Willis DA. Effect of the dielectric transition on laser-induced phase explosion in metals. International Journal of Heat and Mass Transfer 2006;49 (11–12):1928–36.

[22] Lutey AH, Sozzi M, Carmignato S, Selleri S, Cucinotta A, Molari PG. Nanosecond and sub-nanosecond pulsed laser ablation of thin single and multi-layer packaging films. Appl Surf Sci 2013;285:300–8.

[23] Colina M, Molpeceres C, Morales M, Allens-Perkins F, Guadano G, Ocana JL. Laser ablation modelling of aluminium, silver and crystalline silicon for applications in photovoltaic technologies. Surf Eng 2011;27(6):414–23.

[24] Mazzi A, Gorrini F, Miotello A. Liquid nanodroplet formation through phase explosion mechanism in laser-irradiated metal targets. Physical Review E 2015;92 (3):031301.

[25] Kelly R. On the dual role of the Knudsen layer and unsteady, adiabatic expansion in pulse sputtering phenomena. J Chem Phys 1990;92(8):5047–56.

[26] Zhang G, Hua X, Huang Y, Zhang Y, Li F, Shen C, et al. Investigation on mechanism of oxide removal and plasma behavior during laser cleaning on aluminum alloy. Appl Surf Sci 2020;506:144666.

[27] Gragossian A, Tavassoli SH, Shokri B. Laser ablation of aluminum from normal evaporation to phase explosion. J Appl Phys 2009;105(10).

[28] Yoo JH, Jeong SH, Greif R, Russo RE. Explosive change in crater properties during high power nanosecond laser ablation of silicon. J Appl Phys 2000;88(3):1638–49.

[29] Morel V, Bultel A, Chéron BG. The critical temperature of aluminum. International Journal of Thermophysics 2009;30:1853–63.

[30] Lide DR, editor. CRC handbook of chemistry and physics. vol. 85. CRC Press; 2004.

[31] Deierling P, Zhupanska OI, Pasiliao CL. Micromechanical modeling of metal-ceramic composites for high temperature applications. In: 56th AIAA/ASCE/AHS/ASC structures, structural dynamics, and materials conference; 2015. p. 0129.

[32] Kwon H, Yoh JJ. Polarized reflectance of aluminum and nickel to 532, 355 and 266 nm Nd: YAG laser beams for varying surface finish. Optics & Laser Technology 2012;44(6):1823–8.

[33] Gomez-Gesteira M, Rogers BD, Crespo AJ, Dalrymple RA, Narayanaswamy M, Dominguez JM. SPHysics–development of a free-surface fluid solver–part 1: theory and formulations. Comput Geosci 2012;48:289–99.

[34] Xu X, Willis DA. Non-equilibrium phase change in metal induced by nanosecond pulsed laser irradiation. J Heat Transfer 2002;124(2):293–8.

[35] Jafarabadi MA, Mahdieh MH. Investigation of phase explosion in aluminum induced by nanosecond double pulse technique. Appl Surf Sci 2015;346:263–9.

[36] Fishburn JM, Mildren RP, Kapitan D, Withford MJ, Brown DJ, Piper JA. Exploring the explosive ablation regime of metals in nanosecond micromachining. In: High-power laser ablation II. vol. 3885. SPIE; 2000, February. p. 453–60.

[37] Cristoforetti G, Legnaioli S, Palleschi V, Tognoni E, Benedetti PA. Observation of different mass removal regimes during the laser ablation of an aluminium target in air. J Anal At Spectrom 2008;23(11):1518–28.